Electronic Supplementary Material (ESI) for Nanoscale.

Electronic Supplementary Information

Graphene-Ta_2O_5 Heterostructure Enabled High Performance, Deep-Ultraviolet to Mid-Infrared Photodetection

Vinh X. Ho[1], Yifei Wang[1], Michael P. Cooney[2], and Nguyen Q. Vinh[1]*

[1] Department of Physics and Center for Soft Matter and Biological Physics, Virginia Tech, Blacksburg, VA 24061, USA

[2] NASA Langley Research Center, Hampton, Virginia 23681, USA

* Corresponding author: vinh@vt.edu; phone: 1-540-231-3158

1. Device fabrication

The chemical vapor deposition (CVD) monolayer graphene on a copper foil from Graphenea Inc. was transferred onto a Si/SiO_2 substrate.[1-5] A *p*-doped (1 – 10 Ω.cm) Si wafer under a 300-nm-thick SiO_2 layer was used as the back-gate. Metal source and drain contacts (Cr/Au with 10/100-nm thickness) for transport measurements were deposited directly onto the wafer by photolithography to form field effect transistors (FET). The CVD graphene film on top of the wafer was transferred using the poly-(methyl-methacrylate) (PMMA) mediated wet process. The single-layer of graphene was confirmed by the Raman spectroscopy. Using photolithography and oxygen plasma etching processes, graphene films were patterned into different shapes ($W \times L$) on the silicon wafer. L is the gap between drain and contacts (length), and W is the width of the graphene photodetector device (Fig. S1).

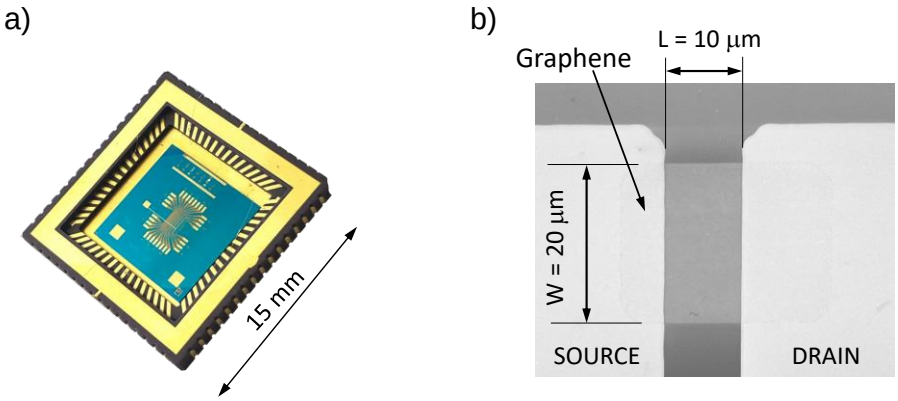

Fig. S1. Images of photodetectors. (a) a picture of photodetector devices including IC package, and (b) a SEM image of an individual photodetector showing the length, *L*, and the width, *W*, of the graphene.

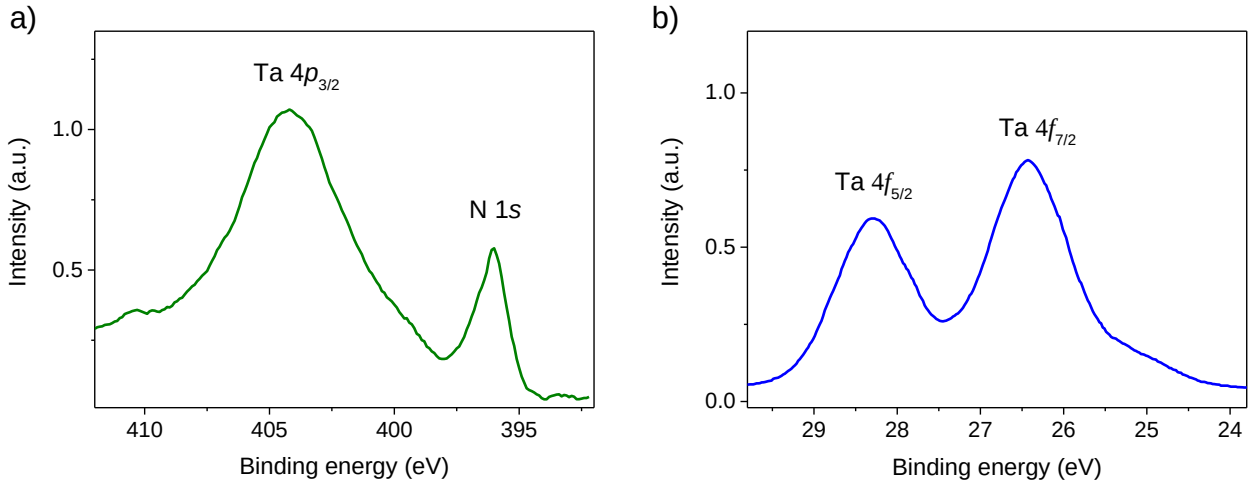

Fig. S2. X-ray photoelectron spectra of N-Ta_2O_5 material (a) Ta 4$p_{3/2}$ and N 1*s* peaks, (b) Ta 4$f_{5/2}$ and 4$f_{7/2}$ peaks.

The orthorhombic-crystalline-structure Ta_2O_5 powder was placed in an alumina crucible and put in the alumina tube furnace. The Ta_2O_5 powder was heated at 750 °C for 2 hours in flowing NH_3 gas at the rate of 100 sccm to obtain the nitrogen-doped tantalum oxide (N-Ta_2O_5) material. The N-Ta_2O_5 was used as a source material to grow the absorber layer on graphene.

The N-Ta_2O_5 material was characterized by X-ray photoelectron spectroscopy (XPS). XPS spectra of the N-Ta_2O_5 material indicate the binding energy of electron for Ta 4$p_{3/2}$ and N 1*s* (Fig. S2a). The XPS peaks for N-doped Ta_2O_5 have been reported in the literature.[6, 7] This is the evidence of nitrogen doped Ta_2O_5 at 750 °C. We applied the XPS at the Ta 4*f* shallow core levels in Fig. S2b. There are two Ta 4$f_{5/2}$ and 4$f_{7/2}$ peaks at 28.3 and 26.4 eV. A tail around 25 eV originates from nitrogen doping to the oxygen vacancy.

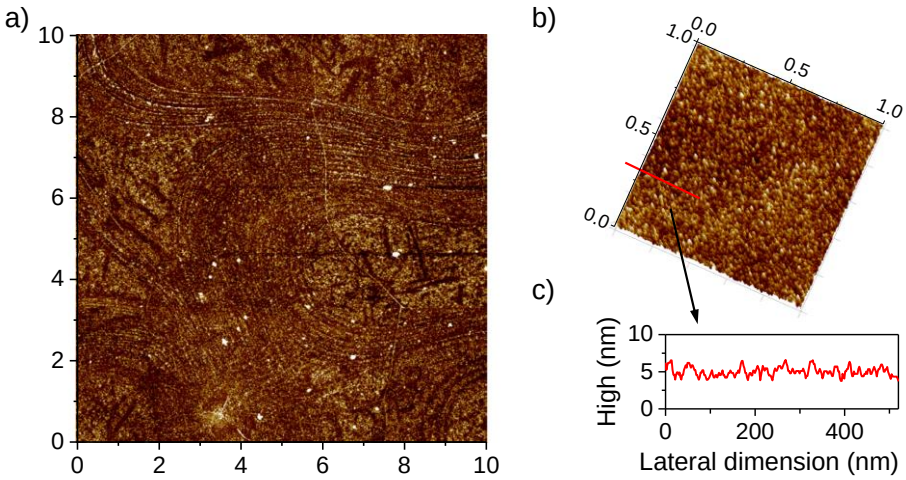

Fig. S3. AFM images of the graphene surface (a), and the N-Ta_2O_5 layer (b) on graphene of photodetector devices.

A 10-nm N-Ta_2O_5 layer was deposited on the CVD graphene by electron-beam thermal evaporation with a slow rate of 0.1 Å/s. This layer acts as a photon absorption material, and contains electron acceptor centers. Then the device was covered with a 30-nm Al_2O_3 dielectric layer using the thermal atomic layer deposition method (ALD) at 250 °C to protect the device from the ambient environment. Figure S1 shows an image of the graphene-Ta_2O_5 photodetector

devices (left) and a scanning electron microscope (SEM) image (right) of an individual photodetector in the main chip.

To verify the quality of the graphene as well as the N-Ta_2O_5 thin film, atomic force microscope (AFM) experiments have been performed. Fig. S3a shows an AFM image of the graphene surface with a size of 10 × 10 μm^2 after the PMMA cleaning process. The graphene surface is homogenous, and there are only a few white dots on the graphene surface in the AFM image. These white dots were originated from PMMA residues, thus almost PMMA residuals were removed in our photodetector devices. An AFM image in Fig. S3b in a short scanning range illustrates the homogeneity of the N-Ta_2O_5 layer with a height of 10 nm.

2. Raman spectrum

To evaluate the quality of graphene after the transferring process, the Raman spectroscopy has been employed. A Raman spectrum (Fig. S4) was obtained by using a WITec UHTS 300 micro-Raman spectrometer equipped with a CCD detector and a 100× objective lens (NA 0.90). The graphene sample was excited by a laser operating at 663.1-nm wavelength. Fig. S4 shows the Raman spectrum of a CVD monolayer graphene on Si/SiO_2. The Raman spectrum shows two main peaks at ~ 1585 cm^{-1} (G line) and ~ 2690 cm^{-1} (2D line). The 2D line is narrow and consists of a single component with a FWHM of 33 cm^{-1}. The intensity ratio of the 2D and G lines, I_{2D}/I_G, is 6.8. The high value confirms a high quality of the graphene layer in the photodetector.[8] The D band around ~ 1350 cm^{-1} (orange box) from graphene defects originating from the graphene transfer process was not observed.[9] These fingerprints provide key evidence of the high-quality of the CVD monolayer graphene, and the efficient transfer process of graphene.

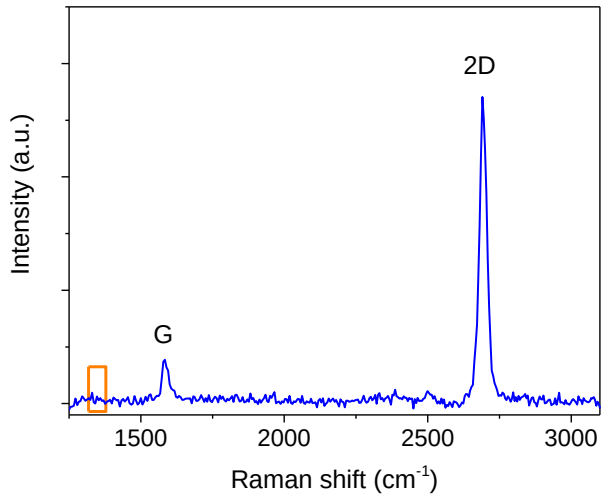

Fig. S4. The Raman spectrum of a CVD monolayer graphene on Si/SiO_2.

3. Absorption measurements

The absorption spectra of the N-Ta_2O_5 material have been recorded from the deep ultraviolet (UV) to mid-infrared (MIR) region (Fig. S5). The Fourier-transform infrared spectroscopy (FTIR) spectrum of the material was recorded on a Nicolet iS50 FTIR spectrometer with a KBr beam splitter (Fig. S5a). The FTIR spectrometer was purged with nitrogen gas for 12 hours to eliminate water vapor and CO_2 before performing absorption measurements. The ultraviolet-visible (UV-VIS) absorption spectra were collected on a Shimadzu UV-3101PC UV-VIS-NIR spectrophotometer. We focus on the optical properties of the N-Ta_2O_5 material using the transmission method. To characterize the optical properties, the material is grown on transmission

substrates. For the visible region, a 100-nm N-Ta_2O_5 material was grown on an α-sapphire thin wafer. Sapphire material has a large bandgap of 8.8 eV,[10] and a wide optical transmission band from the UV to near-infrared (NIR) region. For the infrared region, the material was grown on a thin silicon wafer. To obtain absorption spectra of the material, their substrates have been used for background signals. The configuration of our absorption experiments has been provided in the insets in Fig. S5. UV-VIS absorption spectra of Ta_2O_5 and N-Ta_2O_5 materials have been shown in Fig. S5b. The Tantalum (V) oxide (Ta_2O_5) with 99.99% was purchased from Sigma Aldrich.

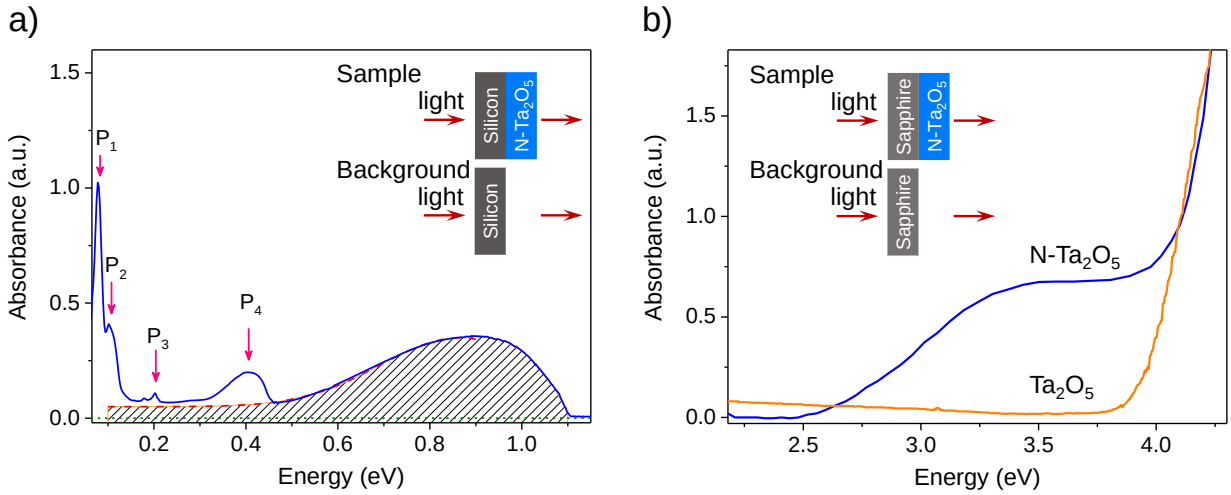

Fig. S5: Absorption spectra of the N-Ta_2O_5 material used in this work. The absorption spectrometers were purged with nitrogen gas to eliminate the contamination of water vapor and CO_2. (a) FTIR spectrum of the N-Ta_2O_5 material on silicon. The red dash-line curve is a Gaussian fitting curve with the peak position over 0.9 eV for the low energy part. Several peaks (P1 to P4) at the low energy part come from vibrational modes in the material. (b) UV-VIS spectra of Ta_2O_5 and N-Ta_2O_5 materials on sapphire.

The absorption spectrum of N-Ta_2O_5 in the NIR region is shown a shoulder at around 0.9 eV, which comes from acceptor centers, and a long tail extending to the MIR region. The red dash-line curve is a Gaussian fitting curve with the peak position at ~ 0.9 eV. The broad band of defect levels near the valence band of N-Ta_2O_5 is supported by calculations of the density-functional theory (DFT).[11, 12] The calculation provides the atomic structure and density of states (DOS) of the defect states of nitrogen-doped Ta_2O_5. This report showed that the substitution of oxygen atoms by nitrogen atoms will remove the oxygen vacancy defect states in the band gap of Ta_2O_5 and leaving nitrogen defect states near the valence band of Ta_2O_5. Therefore, the infrared performance of our photodetector originates from the ionization of acceptor centers with their energy above the valance band. Several peaks (P_1 to P_4) at the low energy part come from vibrational modes in the material, indicating the formation of the Ta_2O_5 material (they are not electronic transitions). These peaks in the absorption spectrum do not involve to the photocurrent. The absorption bands, P_1, at 0.05-0.10 eV (400-800 cm^{-1}) are corresponding to Ta-O-Ta and Ta-O stretching vibrational modes.[13] The peak, P_2, at 0.11 eV (~ 890 cm^{-1}) is assigned with the octahedral units and Ta suboxides. The peak, P_3, at 0.20 eV (1638 cm^{-1}) comes from the in-plane bending vibrations of the Ta-OH groups.[14] The broad peak, P_4, around 0.42 eV (3400 cm^{-1}) corresponds to the stretching frequency of O-H groups.[13, 14] The absorption peaks from the vibrational modes originated from the formation of the N-Ta_2O_5 material do not involve in the photo-response process and thus, we do not discuss the intensity of these peaks.

The absorption of the N-Ta_2O_5 material at the MIR region (low energy part) is a combination of the absorption of defects and vibrational modes of the material (Figure S5b). The defects

cooperate with the photo-response process. The vibration modes (P_1, P_2, P_3, P_4) in the absorption spectrum come from of the N-Ta_2O_5 material. Thus, we need to extract the absorption contribution of the defects. Gaussian function has been used to extract the contribution of the defects in the absorption spectrum. We focused on the MIR region, and this part is not influenced by the absorption of the silicon substrate (E_{gap} = 1.1 eV). The Gaussian fitting curve can extract the low energy part of the absorption peak. In addition to this, the band gap of the N-Ta_2O_5 material becomes narrower (Figure S5b).

4. Electrical and optical measurements

The electrical and optical properties were characterized in a broadband wavelength range at room temperature. A schematics for electrical measurements is shown in Fig. S6 using two Keithley 2400 source-meter units. A source-meter (Keithley 2400) is employed to control the back-gate voltage, V_{BG}. Other source-meter unit (Keithley 2450) is used to set a constant voltage between drain and source, V_{DS}, and to measure the drain current, I_{DS}. To cover a broadband wavelength range from the deep-UV to MIR region, a number of light sources have been used. In the UV-to-NIR region, a UV-VIS broadband light source with a wavelength range from 190 nm to 2.6 μm (Edmund, Deuterium/Tungsten lamp, #87-300), laser diodes operating at 532 and 940 nm, and a fiber laser lasing at 1.53 μm have been employed. For MIR experiments, a quantum cascade laser lasing at 4.55 μm, and a CO_2 laser operating at 10.6 μm are used.

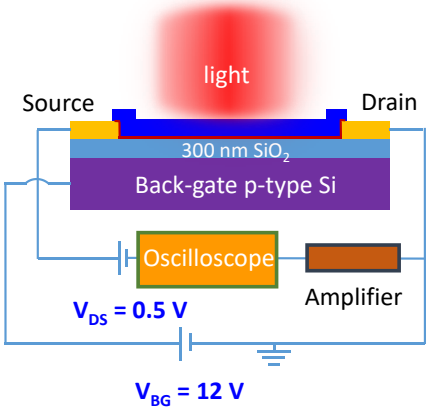

Fig. S6. A Schematic diagram for electrical measurements. A voltage of 0.5 V was applied between drain and source contacts (V_{DS}) using a Keithley 2450 source-meter unit. The back-gate voltage (V_{BG}) was varied from -30 to 30 V with a Keithley 2400 unit. The photocurrent can be collected with a lock-in amplifier, an oscilloscope, or the source-meter unit (Keithley 2450).

To obtain a low and precise power of the light sources on devices, a beam expander has been used. A set of two lenses with f_1 = 25 mm and f_2 = 500 mm (Fig. S7) increases the diameter of a collimated beam. A diaphragm with a 5-mm diameter is used to form the light source with a uniform intensity distribution. A relatively large size of the beam former ensures that we can obtain a correct value of the total power of the beam, and the beam does not contain a significant amount of diffracted light. To verify the uniform intensity distribution, a photodetector with a 10-μm pinhole entrance on a two dimensional stage was used to measure the beam profile. The photon flux of the light sources is measured precisely at the position of our devices with a black anodized aluminum pinhole (1 mm in diameter). A half-wave plate and a polarizing beam-splitter are used to control the power of laser beams. To control the power of incoherent light sources, several sets of Thorlabs neutral density filters have been employed. The light sources cover the entire

graphene FET photodetector. The system allows us to estimate precisely low power of a collimated beam on the graphene-Ta_2O_5 heterostructure photodetectors.[15]

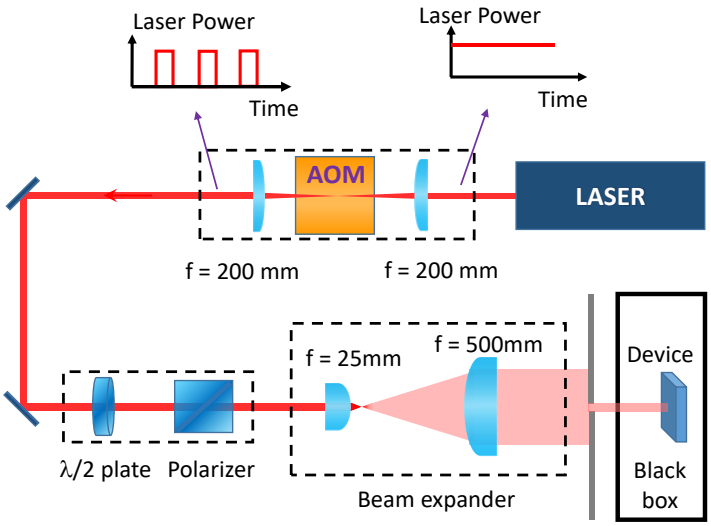

Fig. S7. Optical setup for ultra-fast photo-response measurements. The system consists of an Acousto-optic modulator (AOM), a half-wave plate, a polarizer beam splitter, and lenses. Sample is put in a black box to prevent random light from ambient.

5. Carrier mobility in graphene

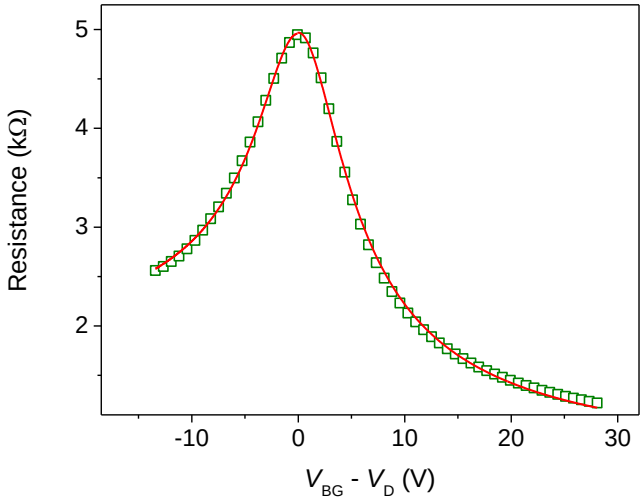

Fig. S8. Resistance – voltage transfer characteristics of a graphene device with N-Ta_2O_5 film (L = 30 μm, W = 30 μm) at room temperature under V_{DS} = 0.1 V.

We determine the mobility, μ, of carriers in graphene from the transfer characteristic curve. The contact resistance, R_c, on a level with the graphene channel resistance, R_{ch}, is estimated from the total device resistance, $R = V_{DS}/I_D$. The mobility of carriers in the graphene device can be extracted by fitting the resistance – voltage (R-V) characteristic curve (Figure 1) in the following form.[16-18]

$$R = 2R_c + R_{ch} = 2R_c + \frac{L}{Wq\mu}\frac{1}{\sqrt{{n_0}^2 + {n_g}^2}}, \quad \text{(S1)}$$

where L = 30 μm and W = 30 μm are the length and width of the graphene channel, respectively, q is the charge of electron, n_0 is the carrier density resulting from charged impurities at the interface between graphene and the SiO_2 dielectric material, $n_g = \frac{C_G}{q}(V_{BG} - V_D)$ is the density of charged carriers generated by a voltage on the back-gate away from the charge neutrality point voltage, V_D, (the Dirac point), $C_G = \frac{\varepsilon\varepsilon_0}{d}$ is the gate capacitance per unit area with d being the thickness of the SiO_2 dielectric material, ε_0 is the vacuum permittivity, and ε ~ 3.9 is the dielectric constant of SiO_2.[19] The capacitance of the 300-nm SiO_2 dielectric layer is ~11.5 nF/cm^2. The red curve in Fig. S8 presents the best fit to the R-V characteristic data using Eq. S1. We obtain the carrier mobility in graphene of ~4890 cm^2/(V·s).

6. Dependence of responsivity on the back-gate voltage

The photo-responsivity of the graphene-Ta_2O_5 heterostructure photodetector can be estimated from the photocurrent and the illumination power. The illumination power was measured with a power meter, and the photocurrent was collected with a lock-in amplifier, an oscilloscope, or the source-meter unit (Keithley 2450). Fig. S9 shows the photo-responsivity of the graphene-Ta_2O_5 heterostructure photodetector ($W \times L$ = 30 × 30 μm^2) as a function of the back-gate voltage, V_{BG}, under 940-nm excitation and V_{DS} = 0.5 V using a lock-in amplifier. Signals collected from source-meter setup and lock-in amplifer are similar. The lock-in setup helps us to have faster measurements.

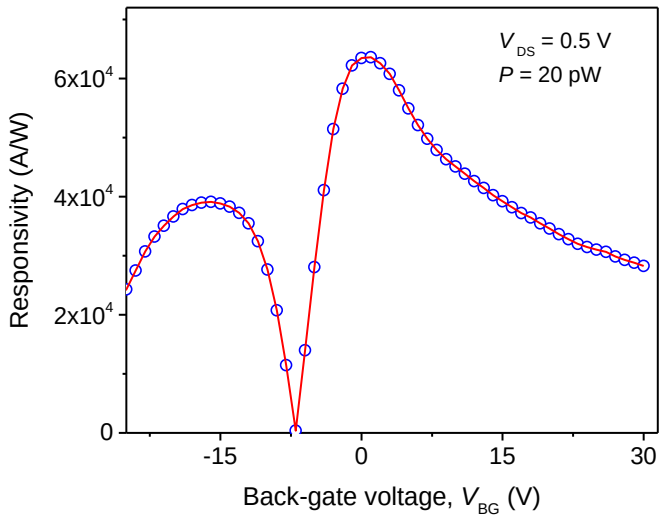

Fig. S9. The photo-responsivity measured with a lock-in system (SR830, Stanford Research) of the graphene-Ta_2O_5 heterostructure photodetector ($W \times L$ = 30 × 30 μm^2) as a function of the back-gate voltage under 940-nm excitation and V_{DS} = 0.5 V.

7. Photocurrent for graphene – Ta_2O_5 devices with different graphene sheet dimensions

The photocurrent of graphene-Ta_2O_5 devices strongly depends on geometrical parameters such as the length, L, and width, W, of the active area. We present the photocurrent as a function of back-gate voltage, V_{BG}, and the illumination power, P. Fig. S10 shows photocurrent functions for (a) $W \times L$= 10 × 20 μm^2; (b) $W \times L$= 20 × 40 μm^2; (c) $W \times L$ = 50 × 100 μm^2; (d) $W \times L$ = 100 × 200 μm^2; and (e) $W \times L$ = 200 × 400 μm^2. Fig. S11 provides photocurrent functions for (a) $W \times L$ = 10 ×10 μm^2; (b) $W \times L$ = 10 × 30 μm^2; (c) $W \times L$ = 10 × 40 μm^2.

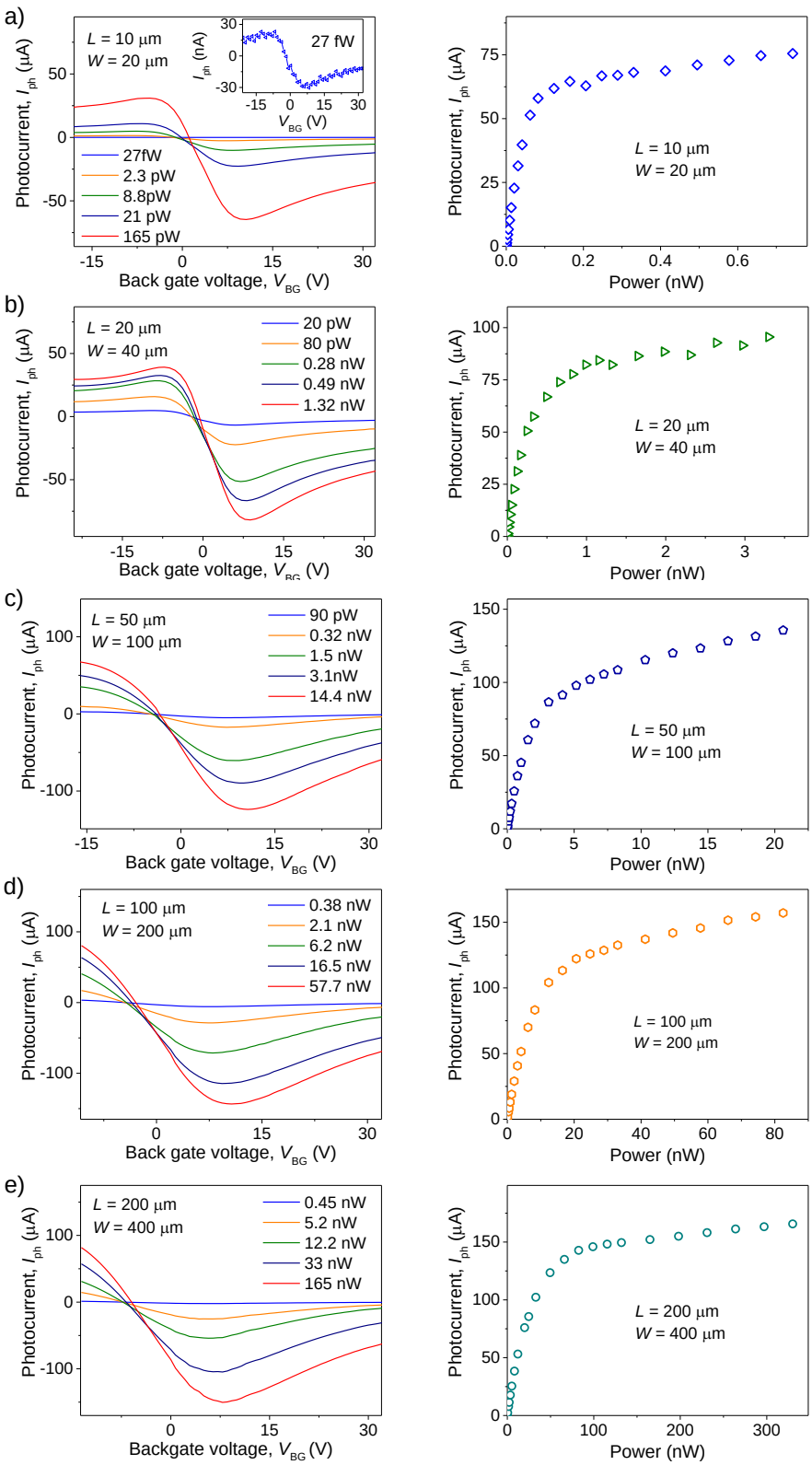

Fig. S10. Photocurrent curves under different illumination powers as a function of back-gate voltage (left), and as a function of illumination power (right) with V_{BG} ~ 7 V for (a) $W \times L$ = 10 × 20 μm^2; (b) $W \times L$ = 20 × 40 μm^2; (c) $W \times L$ = 50 × 100 μm^2; (d) $W \times L$ = 100 × 200 μm^2; and (e) $W \times L$ = 200 × 400 μm^2 under 940-nm excitation and V_{DS} = 0.5 V.

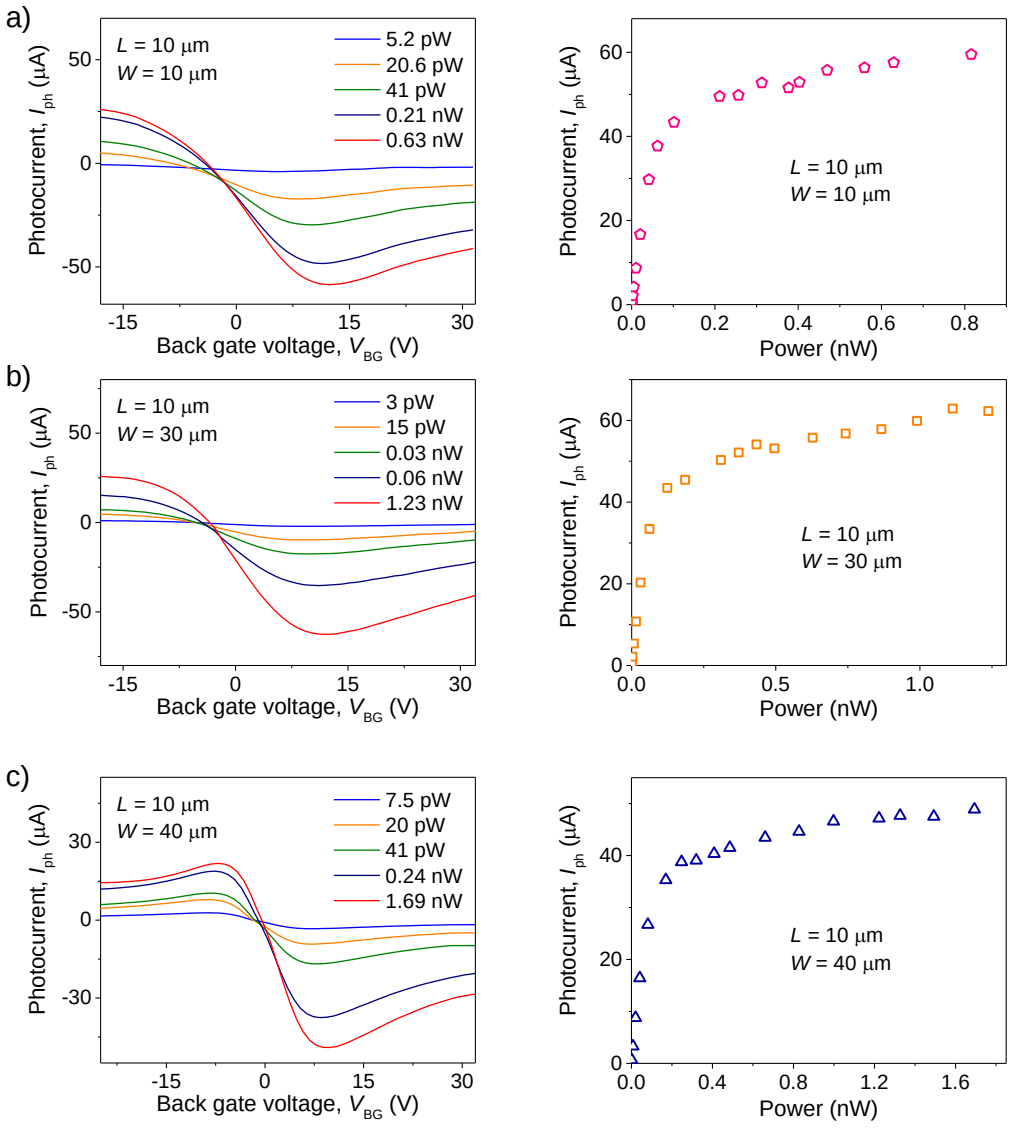

Fig. S11. Photocurrent curves under different illumination powers as a function of back-gate voltage (left), and as a function of illumination power (right) with V_{BG} ~ 7 V for (a) $W \times L$ = 10 × 10 μm^2; (b) $W \times L$ = 10 × 30 μm^2; and (c) $W \times L$ = 10 × 40 μm^2 under 940-nm excitation and V_{DS} = 0.5 V.

8. Power dependence measurements

The photocurrent, I_{ph}, as a function of illumination power with different illumination wavelengths from the deep-UV to MIR region is shown in Fig. S12.

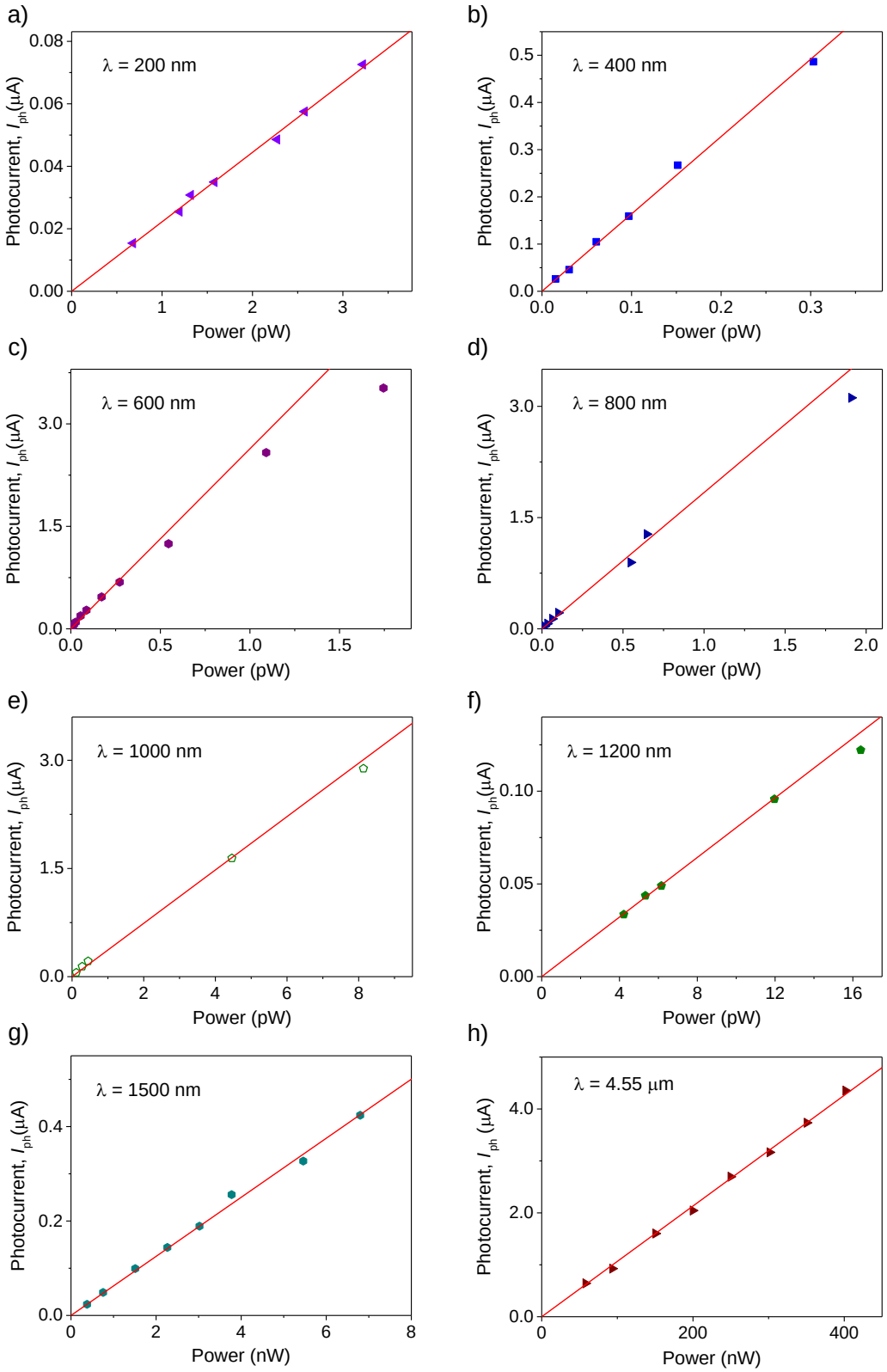

Fig. S12. Photocurrent as a function of illumination power for several light sources with different wavelengths.

9. Noise characterization

For practical applications, the noise-equivalent-power (NEP) as well as the specific detectivity (D^*) are important parameters of a photodetector, which are expressed as

$$D^* = \frac{\sqrt{S \times \Delta f}}{\mathrm{NEP}} \ , \qquad \text{(S2)}$$

where Δf is the bandwidth in hertz, and S is the area of the device in cm^2. The NEP can be evaluated by considering the power spectral density of $1/f$ noise, shot noise, and thermal noise of graphene-Ta_2O_5 photodetectors.

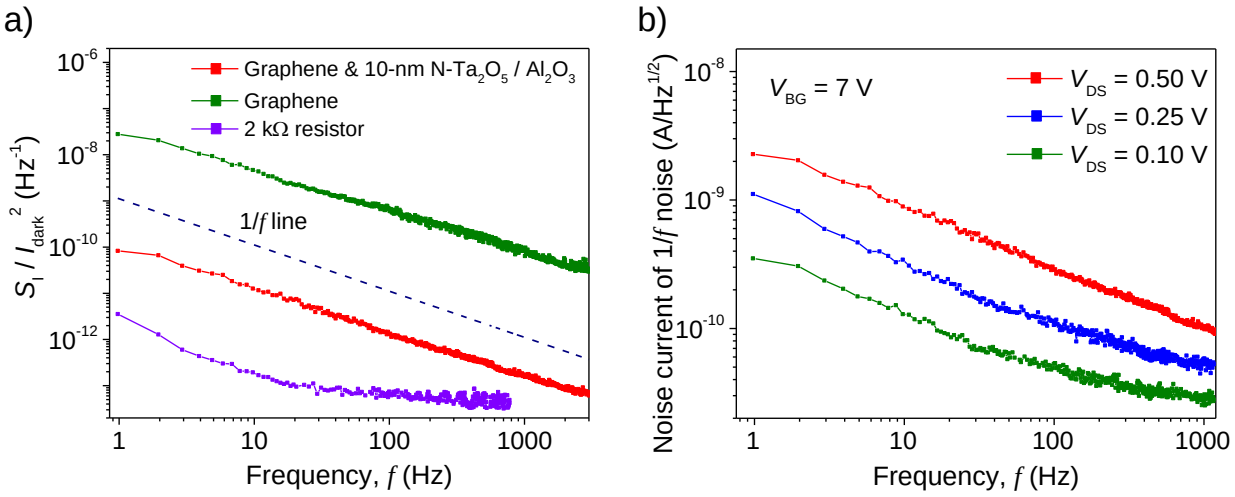

Fig. S13. (a) Normalized noise-power spectral density ($S_\mathrm{I}/I_\mathrm{dark}^2$) of our FET devices with graphene (green curve); the graphene-Ta_2O_5 photodetector ($W \times L$ = 20 × 10 μm^2) with an encapsulated ALD Al_2O_3 layer (red curve) at V_{DS} = 0.5 V and V_{BG} = 7 V at a modulation frequency of 1 Hz. Background noise of our system was characterized with a 2 kΩ resistor (purple). A guide to the eye of the 1/f behavior is shown (dash line with a slope = -1 in the log-log plot). (b) The noise current of $1/f$ noise for the graphene-Ta_2O_5 photodetector with different drain-source voltages, V_{DS}.

The noise-power spectral density is characterized using a single-channel 100 kHz FFT spectrum analyzer (SR770) for the graphene-Ta_2O_5 photodetector with $W \times L$ = 20 × 10 μm^2. The noise-power spectral density was acquired by a current preamplifier with a sampling rate of 1 Hz at V_{DS} = 0.5 V and V_{BG} = 7 V. To evaluate the noise-power spectral density, the power spectral density (S_I) of $1/f$ noise (or the Flicker noise) in the dark can be expressed in term of the normalized noise-power spectral density ($S_\mathrm{I}/I_\mathrm{dark}^2$):[20]

$$S_\mathrm{I}(1/f) = \frac{A I_\mathrm{dark}^2}{f^\beta} \ , \qquad \text{(S3)}$$

where A is the noise amplitude (dimensional less), and β is close to 1. The normalized noise-power spectral density is plotted in Fig. S13a. The spectra are dominated by 1/f noise up to 1 kHz. The normalized noise-power spectral density for a graphene field effect transistor device without the N-Ta_2O_5 layer resembles closely with previous measurements for single-layer graphene devices.[20] Our graphene-Ta_2O_5 photodetectors encapsulated with an ALD Al_2O_3 layer reduce noise by two orders of magnitude. Background noise of our system was characterized

with a 2 kΩ resistor. A similar structure with an encapsulated Al_2O_3 layer shows significantly improvement of the 1/f noise.[21] The noise current of $1/f$ noise, $\sigma(1/f) = \sqrt{S_I(1/f)}$ depends on the bias between drain and source, V_{DS}. Fig. S13b shows the noise current of $1/f$ noise of the graphene-Ta_2O_5 device for three values of V_{DS}. Thus, we have estimated the NEP value from the power spectral density of $1/f$ noise is ~ 2.9 nA/$\sqrt{Hz}$ under V_{DS} = 0.5 V and V_{BG} = 7 V, at a modulation frequency of 1 Hz.

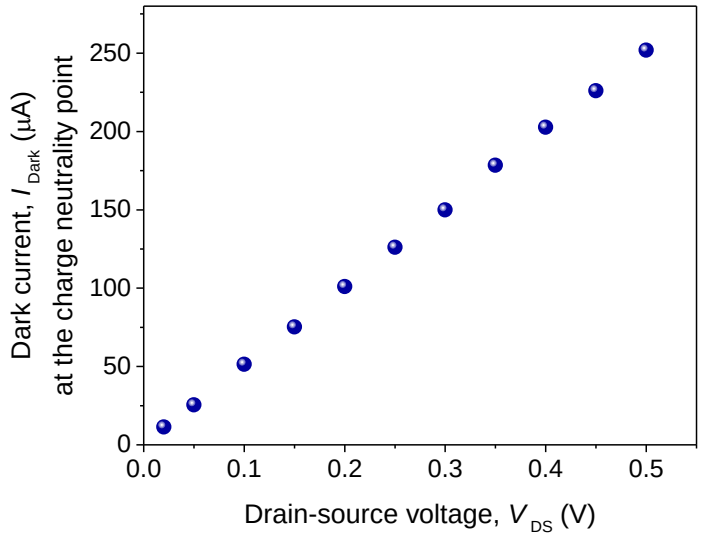

Fig. S14. Dark current at the charge neutrality point as a function of back-gate voltage.

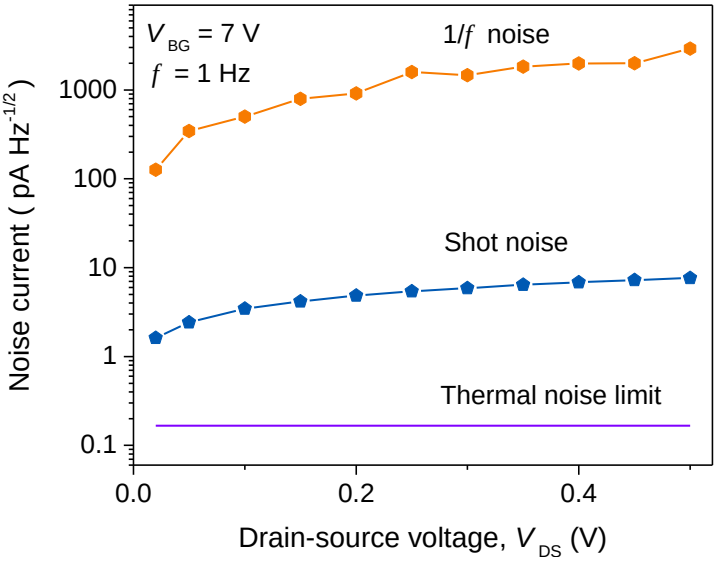

Fig. S15. Noise current of $1/f$ noise, shot noise, and thermal noise of the graphene-Ta_2O_5 photodetector ($W \times L$ = 20 × 10 μm^2) as a function of drain-source voltage, V_{DS}.

The shot noise is estimated from the spectral density of shot noise given by:

$$\sigma_I(\text{shot}) = \sqrt{S_I(\text{shot})} = \sqrt{2qI_{\text{dark}}}\ , \tag{S4}$$

where q is the elemental charge, and I_{dark} is the dark current of the device. Fig. S14 shows the dark current, I_{dark}, at the charge neutrality point as a function of back-gate voltage. The calculated spectral density of shot noise is ~ 7.64 (pA/$\sqrt{\text{Hz}}$).

The thermal noise is calculated from the spectral density of thermal noise by using Nyquist's equation:

$$\sigma_I\ (\text{thermal}) = \sqrt{S_I(\text{thermal})} = \sqrt{4k_BT/R}\ , \tag{S5}$$

where k_B is the Boltzmann's constant, T is the temperature, and R is the differential resistance of the device in the dark. The thermal noise at room temperature is estimated ~ 0.17 (pA/$\sqrt{\text{Hz}}$). The noise current of $1/f$ noise, shot noise, and thermal noise of the graphene-Ta_2O_5 photodetector as a function of drain-source voltage have been presented in Fig. S15.

References

1. K. S. Novoselov, D. Jiang, F. Schedin, T. J. Booth, V. V. Khotkevich, S. V. Morozov and A. K. Geim, *Proc. Natl. Acad. Sci. U. S. A.*, 2005, **102**, 10451-10453.
2. Y. Wang, V. X. Ho, Z. N. Henschel, M. P. Cooney and N. Q. Vinh, *ACS Appl. Nano Mater.*, 2021, **4**, 3647-3653.
3. Y. Wang, V. X. Ho, Z. N. Henschel, P. Pradhan, L. Howe, M. P. Cooney and N. Q. Vinh, *Proc. SPIE*, 2020, **11503**, 1150306.
4. Y. Wang, V. X. Ho, P. Pradhan, M. P. Cooney and N. Q. Vinh, *Proc. SPIE*, 2019, **11088**, 1108809.
5. V. X. Ho, Y. Wang, M. P. Cooney and N. Q. Vinh, *Proc. SPIE*, 2018, **10729**, 1072907.
6. T. Morikawa, S. Saeki, T. Suzuki, T. Kajino and T. Motohiro, *Appl. Phys. Lett.*, 2010, **96**, 142111.
7. T. Murase, H. Irie and K. Hashimoto, *J. Phys. Chem. B*, 2004, **108**, 15803-15807.
8. L. M. Malard, M. A. Pimenta, G. Dresselhaus and M. S. Dresselhaus, *Phys. Rep.*, 2009, **473**, 51-87.
9. M. Her, R. Beams and L. Novotny, *Phys. Lett. A*, 2013, **377**, 1455-1458.
10. R. H. French, *J. Am. Ceram. Soc.*, 1990, **73**, 477-489.
11. N. Sedghi, H. Li, I. F. Brunell, K. Dawson, R. J. Potter, Y. Guo, J. T. Gibbon, V. R. Dhanak, W. D. Zhang, J. F. Zhang, J. Robertson, S. Hall and P. R. Chalker, *Appl. Phys. Lett.*, 2017, **110**, 102902.
12. R. Jinnouchi, A. V. Akimov, S. Shirai, R. Asahi and O. V. Prezhdo, *J. Phys. Chem. C*, 2015, **119**, 26925-26936.
13. J. Y. Zhang, B. Lim and I. W. Boyd, *Thin Solid Films*, 1998, **336**, 340-343.
14. K. Chennakesavulu and G. R. Reddy, *RSC Adv.*, 2015, **5**, 56391-56400.
15. J. R. Mahan, N. Q. Vinh, V. X. Ho and N. B. Munir, *Appl. Opt.*, 2018, **57**, D56-D62.
16. S. Kim, J. Nah, I. Jo, D. Shahrjerdi, L. Colombo, Z. Yao, E. Tutuc and S. K. Banerjee, *Appl. Phys. Lett.*, 2009, **94**, 062107.
17. K. Chen, X. Wan, D. Q. Liu, Z. W. Kang, W. G. Xie, J. Chen, Q. Miao and J. B. Xu, *Nanoscale*, 2013, **5**, 5784-5793.
18. N. Wang, Z. H. Ma, C. Ding, H. Z. Jia, G. R. Sui and X. M. Gao, *Energy Technol.*, 2020, **8**, 1901466.
19. M. Baklanov, M. Green and K. Maex, *Dielectric Films for Advanced Microelectronics*, John Wiley & Sons, Ltd, 2007.
20. M. Kayyalha and Y. P. Chen, *Appl. Phys. Lett.*, 2015, **107**, 113101.
21. S. G. Peng, Z. Jin, D. Y. Zhang, J. Y. Shi, D. C. Mao, S. Q. Wang and G. H. Yu, *ACS Appl. Mater. Interfaces*, 2017, **9**, 6661-6665.